

RESEARCH LETTER

10.1002/2017GL075110

Key Points:

- First cross-validated measurements of the elastic modulus of snow
- Agreement between estimates from P wave propagation and finite element calculations
- A remaining bias between both methods is related to effects of random layering

Supporting Information:

- Supporting Information S1

Correspondence to:

B. Gerling,
bastian.gerling@slf.ch

Citation:

Gerling, B., Löwe, H., & van Herwijnen, A. (2017). Measuring the elastic modulus of snow. *Geophysical Research Letters*, 44, 11,088–11,096. <https://doi.org/10.1002/2017GL075110>

Received 28 JUL 2017

Accepted 19 OCT 2017

Accepted article online 23 OCT 2017

Published online 14 NOV 2017

©2017. The Authors.

This is an open access article under the terms of the Creative Commons Attribution-NonCommercial-NoDerivs License, which permits use and distribution in any medium, provided the original work is properly cited, the use is non-commercial and no modifications or adaptations are made.

Measuring the Elastic Modulus of Snow

B. Gerling¹, H. Löwe¹, and A. van Herwijnen¹
¹WSL Institute for Snow and Avalanche Research SLF, Davos, Switzerland

Abstract The elastic modulus is the most fundamental mechanical property of snow. However, literature values scatter by orders of magnitude and hitherto no cross-validated measurements exists. To this end, we employ P wave propagation experiments under controlled laboratory conditions on decimeter-sized snow specimen, prepared from artificial snow and subjected to isothermal sintering, to cover a considerable range of densities (170–370 kg m⁻³). The P wave modulus was estimated from wave propagation speeds in transverse isotropic media and compared to microstructure-based finite element (FE) calculations from X-ray tomography images. Heterogeneities and size differences between acoustic and FE sample volumes were characterized by SnowMicroPen measurements, yielding an elastic modulus as a by-product. The moduli (10–340 MPa) from the acoustic and FE method are in very good agreement ($R^2 = 0.99$) over the entire range of densities. A remaining bias (24 %) between both methods can be explained by layer heterogeneities which systematically reduce the estimates from the acoustic method.

1. Introduction

The elastic modulus of snow is a fundamental mechanical property relating stress and strain. It is a highly relevant parameter for many snow mechanical application covering engineering aspects of tire traction (Choi et al., 2012), interpretation of seismic waves (Diez et al., 2015), snow fracture in relation to avalanche release (Van Herwijnen et al., 2016), or the validation of new constitutive models (Barracough et al., 2017). Snow is a fragile, porous material that exists close to its melting point, making it highly rate dependent with a strong microstructural influence. Measuring the elastic modulus of snow therefore involves many difficulties (e.g., Mellor, 1975).

Most published values for the elastic modulus of snow were obtained through experiments under controlled laboratory conditions. Summarizing various studies, mostly uniaxial compression experiments at very low strain rates ($\dot{\epsilon} < 4 \times 10^{-4} \text{ s}^{-1}$), Mellor (1975) reported values between 0.2 and 20 MPa for snow densities between 100 and 350 kg m⁻³. More recently, Scapozza (2004) found similar values from quasi-static triaxial compression tests ($\dot{\epsilon} < 10^{-3} \text{ s}^{-1}$). In contrast, by conducting dynamic loading experiments at high strain rates ($\dot{\epsilon} > 10^{-2} \text{ s}^{-1}$), Sigrist (2006) found values between 20 and 70 MPa for snow densities between 210 and 360 kg m⁻³. Elastic modulus values comparable to quasi-static experiments were also obtained from SnowMicroPen (SMP) measurements (Marshall & Johnson, 2009; Reuter et al., 2013), a high-resolution digital cone penetrometer suitable for laboratory or field measurements, or from particle tracking analysis of high-speed photography recordings of field experiments (Van Herwijnen et al., 2016). The observed scatter in published values cannot only be attributed to differences in density, microstructure, or anisotropy and is due to the fact that snow deformation is not purely elastic and includes time dependent viscoplastic components. Indeed, snow only behaves in a linear elastic manner for very high loading rates and/or small deformations below the elastic limit. Values obtained from quasi-static experiments, in particular with strain rates below the ductile-to-brittle transition of snow ($\dot{\epsilon} < 10^{-3} \text{ s}^{-1}$) (e.g., Narita, 1980; Schweizer, 1998), therefore represent effective elastic moduli as time dependent strain components are included.

Amidst the wealth of available methods, wave propagation measurements have also long been used to determine the elastic modulus of snow (Smith, 1965). Since P wave propagation speeds depend on density and elastic moduli, the elastic modulus of snow can be derived from acoustic wave propagation experiments (AC) from first principles and are considered as most consistent (Mellor, 1975) due to high frequencies and small amplitudes. Such experiments invariably result in significantly higher values, on the order of 100 MPa (Capelli et al. 2016; Smith, 1965). Alternatively, the elastic properties can also be derived from finite element

calculations using the reconstructed 3-D microstructure from micro-computed tomography (CT) (e.g., Köhle & Schneebeli, 2014; Schneebeli, 2004; Srivastava et al., 2016; Wautier et al., 2015). This method has become increasingly popular since it is straightforward and reasonably fast. In general, CT-based estimates are comparable to values obtained from P wave propagation experiments. While both measurement methods are assumed to yield true elastic moduli of snow, thus far, no cross-validated measurements exist. The aim of the present letter is therefore to show that measurements of the true elastic modulus of snow are feasible. To this end we present a comparison of AC moduli and CT-based estimates obtained from experiments under controlled laboratory conditions covering a wide range of densities. Additionally, SMP measurements were performed to characterize heterogeneities and size differences between acoustic and CT samples.

2. Methods

2.1. Wave Propagation in Anisotropic, Elastic Continua

Wave propagation in snow as a fluid-filled porous medium should be described within Biot's theory (Johnson, 1982). While the fluid (air) has an effect on attenuation, its impact on propagation velocities of the fast wave is negligible (Capelli et al., 2016), which justifies considering elastic continua to relate velocities and moduli.

The anisotropic microstructure of snow implies anisotropic macroscopic stiffness (e.g., Srivastava et al., 2016), and we assume transverse isotropic (TI) symmetry, a reasonable assumption for snow (Köhle & Schneebeli, 2014; Löwe et al., 2013; Shertzer et al., 2011). Accordingly, the effective stiffness tensor \mathbf{C} of the material has five independent components (Mavko et al., 2009) and in Voigt notation it can be written as

$$\mathbf{C} = \begin{pmatrix} c_{11} & c_{12} & c_{13} & 0 & 0 & 0 \\ c_{12} & c_{11} & c_{13} & 0 & 0 & 0 \\ c_{13} & c_{13} & c_{33} & 0 & 0 & 0 \\ 0 & 0 & 0 & c_{44} & 0 & 0 \\ 0 & 0 & 0 & 0 & c_{44} & 0 \\ 0 & 0 & 0 & 0 & 0 & c_{66} \end{pmatrix}, \quad c_{66} = \frac{1}{2}(c_{11} - c_{12}) \quad (1)$$

In TI media elastic waves can propagate in three different modes and the propagation speed depends on the angle θ between the wave vector and the (vertical) axis of symmetry, involving several components of the stiffness matrix. The propagation speed v of the quasi-longitudinal P wave is given by (Tsvankin, 1996)

$$v = \left(c_{11} \sin^2(\theta) + c_{33} \cos^2(\theta) + c_{44} + \sqrt{A} \right)^{\frac{1}{2}} (2\rho)^{-\frac{1}{2}} \quad (2)$$

in terms of

$$A = [(c_{11} - c_{44}) \sin^2(\theta) - (c_{33} - c_{44}) \cos^2(\theta)]^2 + (c_{13} + c_{44})^2 \sin^2(2\theta) \quad (3)$$

and the density ρ . For longitudinal P waves propagating along the axis of symmetry ($\theta = 0$), equation (2) simplifies to

$$v = \sqrt{\frac{c_{33}}{\rho}} \quad (4)$$

with the P wave modulus c_{33} .

2.2. Snow Sample Preparation and Storage

For the experiments cylindrical samples with a height and diameter of 150 mm were prepared by sieving snow (DFdc, 2mm, Fierz et al., 2009) produced by a snowmaker (Schleef, Jaggi, et al., 2014) into a sample mold. To obtain a wide range of densities, five sieves with different mesh sizes were used in different combinations leading to nine different densities in the range 170–370 kg m⁻³. For each density, two identical samples were prepared. Since CT and SMP are destructive measurements, one sample was used for AC and CT measurements, while the other was used for AC measurements and SMP heterogeneity evaluation. After sieving, the samples were uncased and stored in a closed styrofoam box for 7 days at -5°C before conducting the experiments. The isothermal metamorphism during storage changed the snow type which was classified as RGIr(DF), 0.25–2 mm (Fierz et al., 2009) (cf. Figure 1). An objective characterization by mean and standard deviation of the specific surface area (SSA) for all samples gives $\text{SSA} = 35 \pm 2 \text{ m}^2/\text{kg}$, which is well constrained with only a slight trend of decreasing SSA for higher densities.

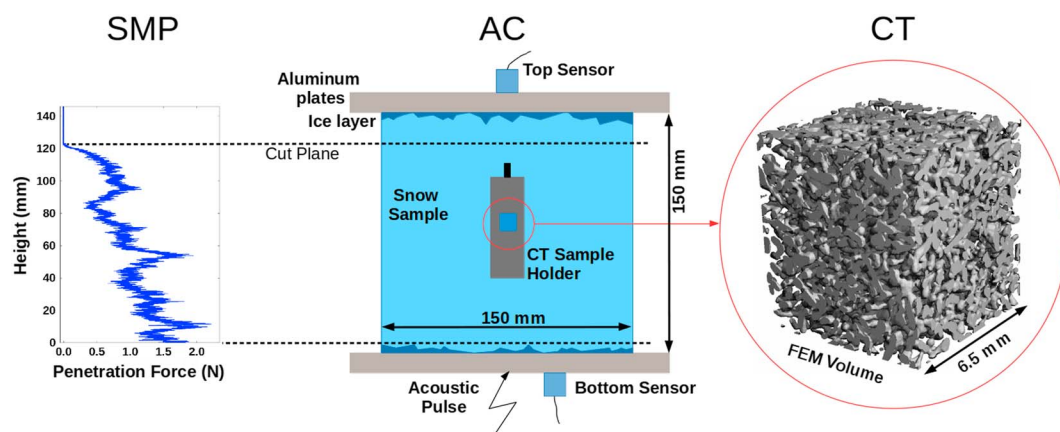


Figure 1. Schematic representation of the measurement setup. (middle) Setup for the acoustic measurements. (left) SnowMicroPen (SMP) measurements, performed in the region indicated by dashed black lines. (right) CT measurement.

The average density for each sample was estimated by a volumetric measurement. Directly after sieving, both identical samples were weighted. The density of the sample after storage was then obtained by measuring the reduction in height of the sample due to densification and will be denoted as ρ^{AC} .

2.3. Acoustic Wave Propagation Measurements

After storage, all samples were prepared for the acoustic measurements conducted in a cold laboratory at a temperature -5°C . To measure wave propagation speeds, aluminum plates were frozen to the top and bottom of the samples (Figure 1). Two wideband differential piezo sensors (MISTRA WD) were attached to the aluminum plates, one to the bottom plate and one to the top plate. The sensor outputs were passed through analog preamplifiers (Mistras/2/4/6) and digitized by 18-bit analog-to-digital converters at a sampling frequency of 2 MHz. To ensure good contact, the sensors were coated with silicon grease and pressed against the plates with a spring. The snow sample was aligned with its axis of symmetry between the top sensor and the location where the acoustic pulse was generated on the bottom plate. The acoustic pulse was generated by knocking on the bottom plate with a metal rod. The input frequency spectrum has a peak frequency in the range 10–20 kHz, and the frequency content of the pulse at the target sensor was generally lower (Figure 2). Note that our experimental setup did not allow for a thorough analysis of the power spectra. This would require a more sophisticated experimental procedure as, for example, used in Capelli et al. (2016).

To determine the wave propagation speed, we used the Akaike Information criterion (Kurz et al., 2005) to identify the onset of the pulse at each sensor, $t_{\text{top}}^{\text{onset}}$ and $t_{\text{bottom}}^{\text{onset}}$, respectively (red and blue dot in Figure 2). The time difference $\Delta t = t_{\text{top}}^{\text{onset}} - t_{\text{bottom}}^{\text{onset}}$ is the sum of the travel time t_{alu} through the aluminum plates and the travel time t_{snow} through snow, $\Delta t = t_{\text{snow}} + t_{\text{alu}}$. The propagation speed is then determined from $v_{\text{snow}} = d/t_{\text{snow}}$ and the height d of the snow sample. At least 10 acoustic pulses were recorded for each sample, and the mean time difference was used to determine v_{snow} . The modulus c_{33}^{AC} was then calculated via equation (4). To assess the uncertainty in c_{33}^{AC} , we accounted for the uncertainty in v_{snow} (5%; minimum 2%, maximum 27%) which incorporates the travel distance uncertainty d (1.3%) and the uncertainty of travel time estimates

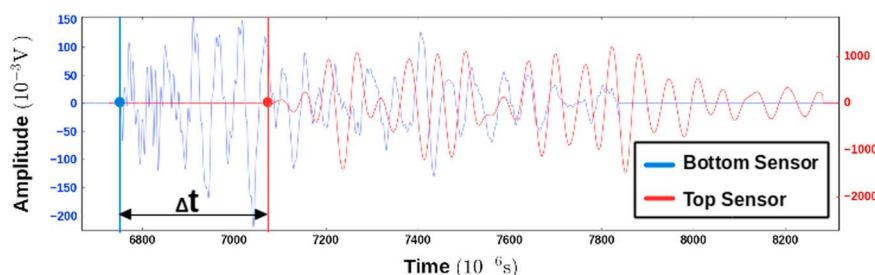


Figure 2. Example (time domain) of the recorded waves in the bottom sensor (blue) and top sensor (red). The detected onset of each pulse is marked with a dot and the travel time is shown.

(5%; minimum 1%, maximum 26%). The latter shows a strong increase for densities below 200 kg m^{-3} (supporting information Figure S4). Combined with the uncertainty in density ρ^{AC} (2%), we derived an overall mean uncertainty of 19% (minimum 7%, maximum 87%) for c_{33}^{AC} . A detailed description of the uncertainty analysis is given in the supporting information (Text S3).

2.4. Micro-Computed Tomography and Finite Element Analysis

For the numerical analysis, cylindrical CT samples were extracted from the middle part of the specimen after the acoustic measurements (Figure 1). The CT samples had a diameter of 18.5 mm and a height of 65 mm, resulting in images with resolution (voxel size) of $(10 \text{ }\mu\text{m})^3$. A Gaussian filter (support 2, $\sigma=1.2$) was applied to the reconstructed grayscale images prior to segmentation. For the analysis, we focused on a cubic region of interest (ROI) (cf. Figure 1, right) with edge length of 6.5 mm (650 voxel). The exponential correlation lengths (Löwe et al., 2013) of all samples, characterized by mean and standard deviation, were $\ell = 58 \pm 5 \text{ }\mu\text{m}$. Thus, the size of the ROI was consistently in the order of $>100\ell$, which is sufficient to meet established requirements on the representative elementary volume (Wautier et al., 2015). The ROI was manually and subjectively chosen by selecting a location of “low vertical heterogeneity” in an overview X-ray image of the full sample. For segmentation, we followed Hagenmüller et al. (2013) and fitted the attenuation histogram of the selected ROI to the sum of three Gaussian distributions for objective thresholding.

The binary image was taken as input for the computation of the elastic moduli by the finite element (FE) method. To this end, we employed the FE code (Garboczi, 1998) for voxel-based microstructures, that is, exactly the same method as used in Srivastava et al. (2016). For the numerical solution the elastic properties of ice were used. As usual for this type of FE analysis, we assume that the ice matrix is made of isotropic, polycrystalline ice and used $K = 8.9 \text{ GPa}$ and $G = 3.5 \text{ GPa}$ (Petrenko & Whitworth, 1999) for bulk and shear modulus, respectively.

From the simulations under different loading conditions, the components c_{11}^{CT} , c_{22}^{CT} , c_{33}^{CT} of the stiffness tensor (equation (1)) were computed to assess the mechanical anisotropy of the sample. Additionally, the underlying structural anisotropy was characterized from the exponential correlation lengths ξ_x^{CT} , ξ_y^{CT} , and ξ_z^{CT} along the three coordinate directions (supporting information Figure S1). The modulus c_{33}^{CT} was compared with the acoustic measurements. Additionally, we compared the CT density ρ^{CT} with ρ^{AC} . To assess the vertical heterogeneity, the microstructure of one snow sample was reconstructed over the entire height by subsampling three overlapping CT samples (supporting information Figure S3). The uncertainty for CT-derived moduli and densities was estimated by conducting sensitivity simulations for selected samples. Varying the segmentation threshold ($\pm 5\%$) yields a variation in density ($\pm 4\%$) and elastic modulus ($\pm 10\%$). Changing the elastic properties of ice to alternative literature values ($K = 9.69 \text{ GPa}$, $G = 3.68 \text{ GPa}$ Northwood, 1947) affected the elastic modulus by 1 to 5% (least and most dense sample, respectively). Finally, the density within scanned volumes show a variation of $\pm 5\%$, which was propagated to an uncertainty for the elastic modulus. Combining the three errors via geometric addition provides the overall uncertainty of the values derived from CT and FE.

2.5. SnowMicroPen Measurements

For the SMP measurements, the aluminum plates were removed after the acoustic measurements and four SnowMicroPen (SMP) measurements (device version 2) were performed (Figure 1). The SMP is a high-resolution digital cone penetrometer specifically tailored to probe the mechanical failure of snow in the penetration direction at high spatial resolution ($4 \text{ }\mu\text{m}$) by using a small cone (5 mm diameter) (Johnson & Schneebeli, 1999). To remove any signal offset, we first subtracted the average force signal measured in the air before the vertical and lateral homogeneity of the samples were quantified as described in supporting information Text S2. In addition, the penetration force resistance signal allows to estimate a density ρ^{SMP} and elastic modulus E^{SMP} . Therefore, three parameters are commonly derived from the penetration resistance: the rupture strength f , the deflection at rupture δ , and the microstructural element length L . We used the shot noise approach by Löwe and van Herwijnen (2012) to extract these parameters from the SMP signal using a moving window of 2.5 mm with 50% overlap. Snow density was estimated from the three microstructural parameters using the parametrization $\rho^{\text{SMP}} = a_1 + a_2 \ln(\bar{F}) + a_3 \ln(\bar{F})L + a_4 L$ suggested by Proksch et al. (2015). Here \bar{F} is the median of the penetration force and the fit parameters are $a_1 = 420.47 \text{ kg m}^{-3}$, $a_2 = 102.47 \text{ N}^{-1}$, $a_3 = -121.15 \text{ N}^{-1} \text{ mm}^{-1}$, and $a_4 = -169.96 \text{ mm}^{-1}$. As a by-product, the SMP analysis also yields an estimate for an elastic modulus as suggested by Johnson and Schneebeli (1999) according to

$$E^{\text{SMP}} = \frac{f}{\delta L}. \quad (5)$$

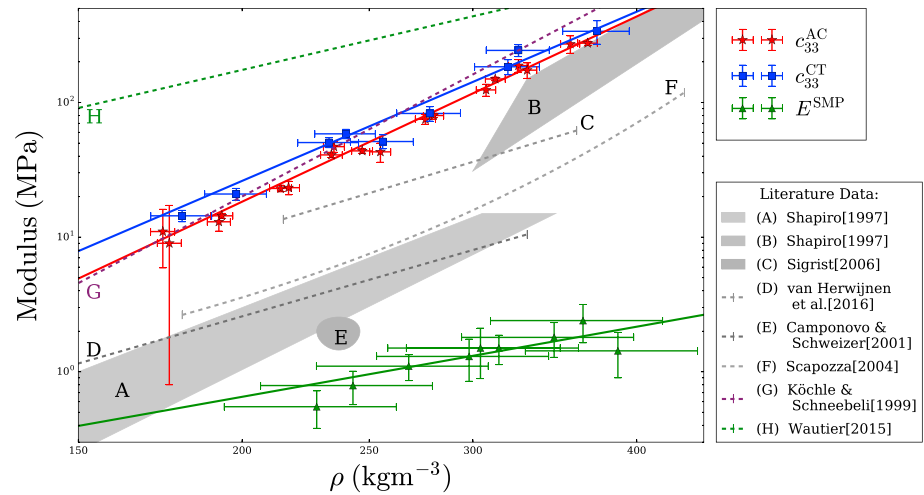


Figure 3. Elastic modulus with snow density. The squares indicate CT data, and the triangles and stars represent the SMP and AC derived data, respectively. A power law function (equation (6)) was used to acquire fits of the elastic modulus to density relationship. Additionally, previously published results are given. The Uniaxial compression and tension experiment moduli (A) and dynamic measurement results (B) are from Shapiro et al. (1997). Experimental-based data are taken from Sigrist (2006) (C), Van Herwijnen et al. (2016) (D), Camponovo and Schweizer (2001) (E), Scapozza (2004) (F), and FE simulation based fits are from Köchle and Schneebeli (2014) (G) and Wautier et al. (2015) (H).

For each moving window, a value for E^{SMP} and ρ^{SMP} was thus obtained. Values reported below are averages over all moving windows and SMP measurements for a specific sample. The uncertainty was estimated as the standard deviations of E^{SMP} and ρ^{SMP} .

3. Results

As expected, the elastic moduli increased with density for all measurement methods (Figure 3). The c_{33}^{CT} values ranged from 14 to 340 MPa and were similar to c_{33}^{AC} values, which ranged from 11 to 275 MPa (blue and red symbols in Figure 3). On the other hand, E^{SMP} values were more than an order of magnitude lower, ranging from 0.6 to 2.4 MPa, and the overall uncertainty in the SMP derived values was much larger (green symbols in Figure 3). Note that the uncertainty in c_{33}^{AC} was very large for the lowest density samples as it was difficult to obtain an accurate onset time at the top sensor due to the strong signal attenuation. The following empirical power laws fitted the experimental data best (lines in Figure 3):

$$\begin{aligned} \text{AC : } c_{33}^{\text{AC}} &= 6 \cdot 10^{-10} (\pm 5 \cdot 10^{-10}) \cdot \rho^{4.60(\pm 0.02)}, & \text{NRMSE} &= 3.5\% \\ \text{CT : } c_{33}^{\text{CT}} &= 2 \cdot 10^{-8} (\pm 4 \cdot 10^{-8}) \cdot \rho^{3.98(\pm 0.03)}, & \text{NRMSE} &= 5.8\% \\ \text{SMP : } E^{\text{SMP}} &= 8 \cdot 10^{-5} (\pm 2 \cdot 10^{-4}) \cdot \rho^{1.7(\pm 0.5)}, & \text{NRMSE} &= 34\% \end{aligned} \quad (6)$$

with NRMSE the normalized root-mean-square error (normalized with the range). Overall, the largest power law exponent was for the AC data, suggesting the strongest increase in elastic modulus with density over the investigated range. Literature values of the power law exponent vary between 2.94 (Sigrist, 2006, high-frequency cyclic loading experiments) and 6.6 (Hagenmuller et al., 2014, numerical simulations), especially the power law fits of Köchle and Schneebeli (2014) and Srivastava et al. (2016), whose FE simulations estimated an exponent of 5.5 and 4.51–4.71, respectively, agreed well. Wautier et al. (2015) found a much lower exponent of 2.34 and attributed the difference to their numerical simulation procedure.

The main result of the paper is the direct comparison of the P wave moduli c_{33}^{AC} and c_{33}^{CT} which are in good agreement (Figure 4a) ($R^2 = 0.99$). Nevertheless, the c_{33}^{CT} values were systematically higher than the c_{33}^{AC} values. Taking CT values as reference, the mean bias was 24 % and the largest deviation was 56 % (blue arrow in Figure 4a). If we exclude the outlier the mean bias reduce to 21% which is, however, still outside the uncertainty range. Such a bias was not observed for the densities, where ρ^{CT} and ρ^{AC} agreed well (mean deviation of 3.3 %; Figure 4b). The largest density mismatch of 15% corresponded again to the sample with the highest overestimated c_{33}^{CT} (blue arrow in Figure 4b).

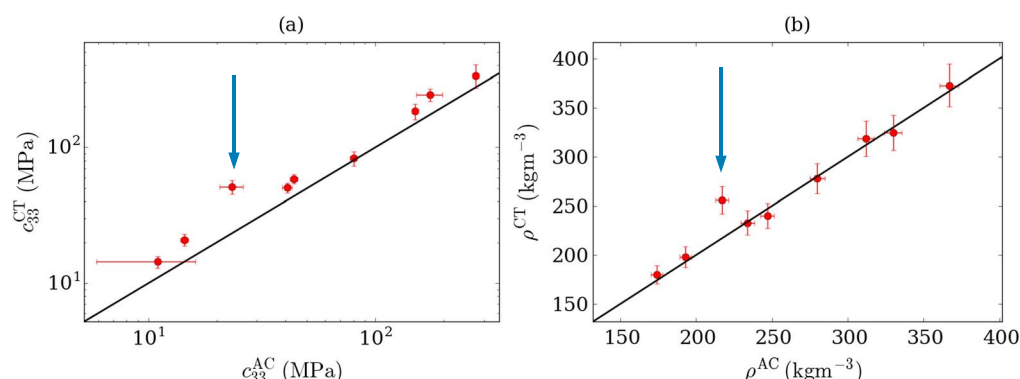


Figure 4. (a) Intercomparison of the elastic moduli derived by CT and AC measurements and (b) the intercomparison of the density. The one-to-one lines serve as a guide for the eye.

4. Discussions

4.1. Impact of Heterogeneities: Scaling Issues

Despite the overall agreement between AC and CT, the comparison revealed a clear bias. The bias did not exhibit a trend with density and was outside the uncertainty range of the measurement methods. We attribute the bias to sample size differences between AC and CT and vertical heterogeneities. The heterogeneity analysis (supporting information Text S2) showed that the AC samples must be regarded as randomly layered media. Random layering also causes TI symmetry which is superimposed on the TI caused by the anisotropic microstructure. For a frequency of 15 kHz and measured wave velocities between 230 and 850 m/s, typical wavelengths range from 1.5 to 5 cm. Hence, in all cases the typical correlation length of the layer structure (≈ 1.8 mm, supporting information Text S2) can be considered small compared to the wavelength and we can resort to Gurevich and Lopatnikov (1995) to assess the implications. When taking the layering into account, the measured velocities for propagation perpendicular to the layers must actually be related to the harmonic mean $\langle c_{33}^{-1} \rangle^{-1}$ of the layer moduli. In contrast, we have manually chosen a ROI for the CT analysis to represent a homogeneous region in the vertical layering. Thus, CT estimates rather correspond to the arithmetic mean $\langle c_{33} \rangle$. This is also confirmed by the fact that the CT density agrees well with the integrated density (approximately to the arithmetic mean) of the entire sample (Figure 4b). The two different averages are related by the Jensen inequality $\langle c_{33}^{-1} \rangle^{-1} \leq \langle c_{33} \rangle$ suggesting that AC moduli are always smaller. An order of magnitude of this effect can be estimated by combining the fit $c_{33}^{\text{CT}}(\rho)$ from equation (6) with the total CT density profile $\rho(z)$ (supporting information Figure S3) and computing the respective averages by vertically integrating over the full sample depth. The result reveals that $\langle c_{33}^{-1} \rangle^{-1}$ is 12% lower than $\langle c_{33} \rangle$, providing an explanation for the direction and order of magnitude of the observed bias between AC and CT.

4.2. Methodological Limitations

We devised a sample preparation and storage method allowing us to cover a wide range of densities, which are, however, still limited in scope. The upper limit was constrained by the snow type used for sample preparation since snow morphology should not change over the entire density range. The lowest density, on the other hand, was limited by the AC measurement system as it was not possible to detect acoustic pulses that propagated through snow samples with a density $< 150 \text{ kg m}^{-3}$. As a consequence, travel time uncertainties increase for densities $< 200 \text{ kg m}^{-3}$ due to the reduction of the signal-to-noise ratio from the target sensor (supporting information Figure S4). A remedy would be to reduce the sample height. However, this would increase the uncertainty in the elastic modulus as the relative error in the onset picking would increase for shorter propagation lengths as well. A more sensitive AC measurement system, in particular a more sensitive sensor and a more energetic pulse, would thus be required to extend the density range to lower densities or reduce the sample size.

For the CT analysis, the choice of the segmentation procedure has a substantial influence on the derived parameters (Hagenmüller et al., 2016). We also tried a manual segmentation (Iassonov et al., 2009) for the entire data set, which resulted in a systematic underestimation of the c_{33}^{CT} by -19% . However, the objective nature of the present segmentation (Hagenmüller et al., 2013) (cf. section 2.4) together with the good agreement for the density with the volumetric measurements (Figure 4b) provides a fair amount of confidence in the results.

Finally, SMP estimates for the moduli must be regarded as non-competitive since the modulus equation (5) (Johnson & Schneebeli, 1999) lacks a sound theoretical justification. The poor agreement between the E^{SMP} and c_{33}^{AC} values indicate that E^{SMP} is an effective, microscale quantity. The observed discrepancies between the moduli, by up to 2 orders of magnitude, are comparable to recently published results by Capelli et al. (2016) and Reuter et al. (2013). To obtain realistic moduli from SMP measurements, a more physically based model has to be developed which accounts for material compaction and finite size effects at the SMP tip (Johnson, 2003; Ruiz et al., 2017; van Herwijnen, 2013).

4.3. Relevance of the Results

Within the limitations of the methods and issues of heterogeneity discussed above, our results suggest that both, AC and CT, estimate the same property, namely, the true elastic modulus of snow. This has some implications on existing work and opens new routes for applications.

While our experiments were limited to a single snow type (RG), CT moduli for other snow types are widely available (e.g., Köchle & Schneebeli, 2014; Schneebeli, 2004; Srivastava et al., 2016; Wautier et al., 2015) and can be used to further discuss effects of microstructure on the true elastic modulus. Apart from the first order effect of density on the elastic modulus, second order effects of microstructure are well known (e.g., Köchle & Schneebeli, 2014; Mellor, 1975; Srivastava et al., 2016; Shapiro et al., 1997). Due to gravity and temperature gradients pronounced, differences of the modulus in directions parallel and perpendicular to the vertical (Srivastava et al., 2016) should always be expected, even for putatively idealized conditions as in the present case (supporting information Text S1). It remains an open question though, under which conditions the assumed TI symmetry of the stiffness tensor (section 2) should be replaced by a full orthotropic symmetry (Srivastava et al., 2016; Wautier et al., 2015).

While the level of detail and the additional parameters which can be derived from CT imaging remain unparalleled, the AC method also has some practical advantages. With some further development, a field applicable device to measure the elastic modulus of natural snow layers is conceivable. In addition, the acoustic wave propagation method can be used to perform rapid, repeated measurements. This makes it an optimal method to investigate the temporal evolution of elastic properties at short time scales, for instance, during metamorphism, settlement or sintering (e.g., Schleef, Löwe, et al., 2014; van Herwijnen & Miller, 2013). Thereby, AC measurements can be used to investigate combined effects of structural and layer anisotropy by performing wave propagation measurements along different directions to compute additional terms of the elastic stiffness tensor (Castagnede et al., 1990; Tsvankin, 1996). The ease of use, relative low cost, and potential field application make the AC method particularly well suited to establish empirical parameterizations for the elastic modulus with density and snow morphology, which would be of great interest to various applications, from the interpretation of seismic borehole data in polar ice sheets (e.g., Diez et al., 2015) to snow avalanche forecasting (e.g., Gaume et al., 2017).

5. Conclusions

We performed laboratory measurements to compare the P wave modulus c_{33} of snow from acoustic wave propagation measurements (AC) with micro-computed tomography based finite element calculations (CT). A third modulus was derived from high-resolution digital cone penetrometer measurements (SMP) which were employed to characterize sample heterogeneities. To the best of our knowledge, our results provide the first direct comparison of independent measurement methods for the elastic modulus of snow. The absolute values of AC and CT derived moduli, ranging from 11 to 340 MPa, agreed well over the entire density range. SMP derived values, on the other hand, were up to 2 orders of magnitude lower (0.6 to 2.4 MPa). The observed bias between AC and CT was attributed to layer heterogeneities, which effectively reduce the AC modulus measured on decimeter scale over the millimeter-scale estimates from CT. The results confirm that the true (high-frequency, small strain) elastic modulus of snow is fairly high and should be distinguished from measurements which are likely affected by the viscoplasticity of ice.

References

- Barracough, T., Blackford, J. R., Liebenstein, S., Sandfeld, S., Stratford, T. J., Weinlaender, G., & Zaiser, M. (2017). Propagating compaction bands in confined compression of snow. *Nature Physics*, 13(3), 272–275. <https://doi.org/10.1038/NPHYS3966>
- Campanovo, C., & Schweizer, J. (2001). Rheological measurements of the viscoelastic properties of snow. *Annals of Glaciology*, 32, 44–50. <https://doi.org/10.3189/172756401781819148>

Acknowledgments

All data for the present work are available upon request from the corresponding author. This work was partly funded through Swiss National Science Foundation (grant 200021_16942). The authors thank two anonymous reviewers for their constructive feedback on the manuscript.

- Capelli, A., Kapil, J. C., Reiweger, I., Or, D., & Schweizer, J. (2016). Speed and attenuation of acoustic waves in snow: Laboratory experiments and modeling with Biot's theory. *Cold Regions Science and Technology*, 125, 1–11. <https://doi.org/10.1016/j.coldregions.2016.01.004>
- Castagnede, B., Jenkins, J., Sachse, W., & Baste, S. (1990). Optimal determination of the elastic-constants of composite-materials from ultrasonic wave-speed measurements. *Journal of Applied Physics*, 67(6), 2753–2761. <https://doi.org/10.1063/1.345441>
- Choi, J., Cho, J., Woo, J., & Kim, K. (2012). Numerical investigation of snow traction characteristics of 3-D patterned tire. *Journal of Terramechanics*, 49(2), 81–93. <https://doi.org/10.1016/j.jterra.2012.01.003>
- Diez, A., Eisen, O., Hofstede, C., Lambrecht, A., Mayer, C., Miller, H., ... Weikusat, I. (2015). Seismic wave propagation in anisotropic ice—Part 2: Effects of crystal anisotropy in geophysical data. *The Cryosphere*, 9(1), 385–398. <https://doi.org/10.5194/tc-9-385-2015>
- Fierz, C., Armstrong, R., Durand, Y., Etchevers, P., Greene, E., McClung, D., ... Sokratov, S. (2009). *The international classification for seasonal snow on the ground, HP-VII technical documents in hydrology* (Vol. 83, 90 pp.). Paris, France: UNESCO-IHP.
- Garboczi, E. (1998). Finite element and finite difference programs for computing the linear electrical and elastic properties of digital images of random materials (Report NISTIR 6269). Gaithersburg, MD: National Institute for Standards and Technology, U.S. Department of Commerce.
- Gaume, J., van Herwijnen, A., Chambon, G., Wever, N., & Schweizer, J. (2017). Snow fracture in relation to slab avalanche release: Critical state for the onset of crack propagation. *Cryosphere*, 11(1), 217–228. <https://doi.org/10.5194/tc-11-217-2017>
- Gurevich, B., & Lopatnikov, S. (1995). Velocity and attenuation of elastic-waves in finely layered porous rocks. *Geophysical Journal International*, 121(3), 933–947. <https://doi.org/10.1111/j.1365-246X.1995.tb06449.x>
- Hagenmuller, P., Chambon, G., Lesaffre, B., Flin, F., & Naaim, M. (2013). Energy-based binary segmentation of snow microtomographic images. *Journal of Glaciology*, 59(217), 859–873. <https://doi.org/10.3189/2013JoG13J035>
- Hagenmuller, P., Calonne, N., Chambon, G., Flin, F., Geindreau, C., & Naaim, M. (2014). Characterization of the snow microstructural bonding system through the minimum cut density. *Cold Regions Science and Technology*, 108, 72–79. <https://doi.org/10.1016/j.coldregions.2014.09.002>
- Hagenmuller, P., Matzl, M., Chambon, G., & Schneebeli, M. (2016). Sensitivity of snow density and specific surface area measured by microtomography to different image processing algorithms. *Cryosphere*, 10(3), 1039–1054. <https://doi.org/10.5194/tc-10-1039-2016>
- Iassonov, P., Gebrenegus, T., & Tuller, M. (2009). Segmentation of X-ray computed tomography images of porous materials: A crucial step for characterization and quantitative analysis of pore structures. *Water Resources Research*, 45, W09415. <https://doi.org/10.1029/2009WR008087>
- Johnson, J. (2003). A statistical micromechanical theory of cone penetration in granular materials (ERDC/CRREL Technical Report, ERDC/CRREL-TR-03-3 U.S.). Hanover, NH: Army Corps of Engineers, Engineer Research and Development Center.
- Johnson, J., & Schneebeli, M. (1999). Characterizing the microstructural and micromechanical properties of snow. *Cold Regions Science and Technology*, 30(1–3), 91–100. [https://doi.org/10.1016/S0165-232X\(99\)00013-0](https://doi.org/10.1016/S0165-232X(99)00013-0)
- Johnson, J. B. (1982). On the application of Biot's theory to acoustic wave propagation in snow. *Cold Regions Science and Technology*, 6(1), 49–60. [https://doi.org/10.1016/0165-232X\(82\)90044-1](https://doi.org/10.1016/0165-232X(82)90044-1)
- Köchle, B., & Schneebeli, M. (2014). Three-dimensional microstructure and numerical calculation of elastic properties of alpine snow with a focus on weak layers. *Journal of Glaciology*, 60(222), 705–713. <https://doi.org/10.3189/2014JoG13J220>
- Kurz, J. H., Grosse, C. U., & Reinhardt, H.-W. (2005). Strategies for reliable automatic onset time picking of acoustic emissions and of ultrasound signals in concrete. *Ultrasonics*, 43(7), 538–546. <https://doi.org/10.1016/j.ultras.2004.12.005>
- Löwe, H., & van Herwijnen, A. (2012). A Poisson shot noise model for micro-penetration of snow. *Cold Regions Science and Technology*, 70, 62–70. <https://doi.org/10.1016/j.coldregions.2011.09.001>
- Löwe, H., Riche, F., & Schneebeli, M. (2013). A general treatment of snow microstructure exemplified by an improved relation for thermal conductivity. *The Cryosphere*, 7, 1473–1480. <https://doi.org/10.5194/tc-7-1473-2013>
- Marshall, H., & Johnson, J. B. (2009). Accurate inversion of high-resolution snow penetrometer signals for microstructural and micromechanical properties. *Journal of Geophysical Research*, 114, F04016. <https://doi.org/10.1029/2009JF001269>
- Mavko, G., Mukerji, T., & Dvorkin, J. (2009). *The rock physics handbook* (2nd ed., p. 524). Cambridge, UK: Cambridge University Press. <https://doi.org/10.1017/CBO9780511626753>
- Mellor, M. (1975). A review of basic snow mechanics, *Symposium at Grindelwald 1974—Snow mechanics* (vol. 114, pp. 251–291), International Association of Hydrological Sciences. Wallingford, UK: IAHS Publication.
- Narita, H. (1980). Mechanical behaviour and structure of snow under uniaxial tensile stress. *Journal of Glaciology*, 26(94), 275–282. <https://doi.org/10.3189/S0022143000010819>
- Northwood, T. D. (1947). Sonic determination of the elastic properties of ice. *Canadian Journal of Research*, 25(2), 88–95. <https://doi.org/10.1139/cjr47a-011>
- Petrenko, V., & Whitworth, R. (1999). *Physics of ice* (p. 373). Oxford, UK: Oxford University Press Inc. <https://doi.org/10.1093/acprof:oso/9780198518945.001.0001>
- Proksch, M., Löwe, H., & Schneebeli, M. (2015). Density, specific surface area and correlation length of snow measured by high-resolution penetrometry. *Journal of Geophysical Research: Earth Surface*, 120, 346–362. <https://doi.org/10.1002/2014JF003266>
- Reuter, B., Proksch, M., Löwe, H., van Herwijnen, A., & Schweizer, J. (2013). On how to measure snow mechanical properties relevant to slab avalanche release, *International snow science workshop Grenoble, France, 7–11 October, 2013* (pp. 7–11). Grenoble, France: ANENA, IRSTEA, METEO-France.
- Ruiz, S., Capelli, A., van Herwijnen, A., Schneebeli, M., & Or, D. (2017). Continuum cavity expansion and discrete micromechanical models for inferring macroscopic snow mechanical properties from cone penetration data. *Geophys. Research Letters*, 44, 8377–8386. <https://doi.org/10.1002/2017GL074063>
- Scapozza, C. (2004). Entwicklung eines dichte- und temperaturabhängigen stoffgesetzes zur beschreibung des visko-elastischen verhaltens von schnee (PhD Thesis), ETH Zürich.
- Schleef, S., Jaggi, M., Löwe, H., & Schneebeli, M. (2014). An improved machine to produce nature-identical snow in the laboratory. *Journal of Glaciology*, 60(219), 94–102. <https://doi.org/10.3189/2014JoG13J118>
- Schleef, S., Löwe, H., & Schneebeli, M. (2014). Hot-pressure sintering of low-density snow analyzed by X-ray microtomography and in situ microcompression. *Acta Materialia*, 71, 185–194. <https://doi.org/10.1016/j.actamat.2014.03.004>
- Schneebeli, M. (2004). Numerical simulation of elastic stress in the microstructure of snow. *Annals of Glaciology*, 38, 339–342. <https://doi.org/10.3189/172756404781815284>
- Schweizer, J. (1998). Laboratory experiments on shear failure of snow. *Annals of Glaciology*, 26, 97–102. <https://doi.org/10.3189/1998AoG26-1-97-102>
- Shapiro, L., Johnson, J., Sturm, M., & Blaisdell, G. (1997). Snow mechanics—Review of the state of knowledge and applications (Research Report 97). Hanover, NH: USA Cold Regions Research and Engineering Laboratory.

- Shertzer, R. H., Adams, E. E., & Schneebeli, M. (2011). Anisotropic thermal conductivity model for dry snow. *Cold Regions Science and Technology*, 69(2–3), 122–128. <https://doi.org/10.1016/j.coldregions.2011.09.005>
- Sigrist, C. (2006). *Measurement of fracture mechanical properties of snow and application to dry snow slab avalanche release*. ETH Zürich: PhD thesis.
- Smith, J. L. (1965). The elastic constants, strength and density of Greenland snow as determined from measurements of sonic wave velocity (*Research Report 167*). Hanover, NH: US Army Cold Regions Research and Engineering Laboratory.
- Srivastava, P. K., Chandel, C., Mahajan, P., & Pankaj, P. (2016). Prediction of anisotropic elastic properties of snow from its microstructure. *Journal of Cold Regions Engineering*, 125, 85–100. <https://doi.org/10.1016/j.coldregions.2016.02.002>
- Tsvankin, I. (1996). P-wave signatures and notation for transversely isotropic media: An overview. *Geophysics*, 61(2), 467–483. <https://doi.org/10.1190/1.1443974>
- van Herwijnen, A. (2013). Experimental analysis of snow micropenetrometer (SMP) cone penetration in homogeneous snow layers. *Canadian Geotechnical Journal*, 50(10), 1044–1054. <https://doi.org/10.1139/cgj-2012-0336>
- van Herwijnen, A., & Miller, D. A. (2013). Experimental and numerical investigation of the sintering rate of snow. *Journal of Glaciology*, 59(214), 269–274. <https://doi.org/10.3189/2013JoG12J094>
- Van Herwijnen, A., Gaume, J., Bair, E. H., Reuter, B., Birkeland, K. W., & Schweizer, J. (2016). Estimating the effective elastic modulus and specific fracture energy of snowpack layers from field experiments. *Journal of Glaciology*, 62(236), 997–1007. <https://doi.org/10.1017/jog.2016.90>
- Wautier, A., Geindreau, C., & Flin, F. (2015). Linking snow microstructure to its macroscopic elastic stiffness tensor: A numerical homogenization method and its application to 3-D images from X-ray tomography. *Geophys Research Letters*, 42, 8031–8041. <https://doi.org/10.1002/2015GL065227>